Energy & Environmental Science

ROYAL SOCIETY OF CHEMISTRY

PAPER

View Article Online
View Journal | View Issue

Cite this: *Energy Environ. Sci.*, 2024, **17**, 2530

Does trapped O_2 form in the bulk of $LiNiO_2$ during charging?†

Mikkel Juelsholt, ‡[a] Jun Chen, ‡[a] Miguel A. Pérez-Osorio,[ab] Gregory J. Rees,[ab] Sofia De Sousa Coutinho,[ab] Helen E. Maynard-Casely,[c] Jue Liu,[d] Michelle Everett,[d] Stefano Agrestini,[e] Mirian Garcia-Fernandez,[e] Ke-Jin Zhou,[e] Robert A. House *[ab] and Peter G. Bruce *[abf]

Received 15th December 2023,
Accepted 26th February 2024

DOI: 10.1039/d3ee04354a

rsc.li/ees

$LiNiO_2$ remains a critical archetypal material for high energy density Li-ion batteries, forming the basis of Ni-rich cathodes in use today. Nevertheless, there are still uncertainties surrounding the charging mechanism at high states of charge and the potential role of oxygen redox. We show that oxidation of O^{2-} across the 4.2 V *vs.* Li^+/Li plateau forms O_2 trapped in the particles and is accompanied by the formation of 8% Ni vacancies on the transition metal sites of previously fully dense transition metal layers. Such Ni vacancy formation on charging activates O-redox by generating non-bonding O 2p orbitals and is necessary to form vacancy clusters to accommodate O_2 in the particles. Ni accumulates at and near the surface of the particles on charging, forming a Ni-rich shell approximately 5 nm thick; enhanced by loss of O_2 from the surface, the resulting shell composition is $Ni^{2.3+}{}_{1.75}O_2$. The overall Ni oxidation state of the particles measured by XAS in fluorescence yield mode after charging across the plateau to 4.3 V *vs.* Li^+/Li is approximately +3.8; however, taking account of the shell thickness and the shell Ni oxidation state of +2.3, this indicates a Ni oxidation state in the core closer to +4 for compositions beyond the plateau.

Broader context

Li-ion batteries are a critical part of global efforts to decarbonise our transport systems thanks to the high energy densities they offer. One of the key factors limiting the amount of energy that Li-ion batteries can store is the cathode, typically a lithium transition metal oxide, *e.g.* $LiNi_{1/3}Mn_{1/3}Co_{1/3}O_2$. Efforts to further improve these materials and reduce their Co contents lead naturally towards more Ni-rich cathodes, the ultimate example of which is $LiNiO_2$. Unfortunately, $LiNiO_2$ suffers from a number of problems at high states of charge which have been linked with oxygen redox. The phenomenon of oxygen redox is well known in so-called Li-rich transition metal oxide cathodes, where on charge, O^{2-} is oxidised to form molecular O_2 trapped within the structure. However, whether this same mechanism extends to materials with fully dense transition metal layers such as $LiNiO_2$ has been a topic of recent debate. Here, we show that trapped O_2 does form in $LiNiO_2$, accommodated by Ni vacancies that form in transition metal layers on charging. These results represent an important step towards a universal understanding of oxygen redox, which is critical for developing new high-energy density cathodes.

Introduction

Ni-rich cathodes, such as $LiNi_{0.8}Mn_{0.1}Co_{0.1}O_2$, currently offer the best-in-class energy density in Li-ion batteries. In the drive to remove Co from these cathodes, it is critical to understand the behaviour of the ultimate Ni-rich archetype, $LiNiO_2$.[1–5] At high states of charge, $LiNiO_2$ exhibits O-loss, a contraction in interlayer spacing, particle cracking and poor cycling stability.[5–12] Substantial efforts have been made to understand these phenomena and the structural transitions that take place when Li is extracted from $LiNiO_2$, but there remains considerable debate over the extent of Ni oxidation and O-redox in $LiNiO_2$, particularly across the voltage plateau at 4.2 V *vs.* Li^+/

[a] *Department of Materials, University of Oxford, Oxford, UK. E-mail: robert.house@materials.ox.ac.uk, peter.bruce@materials.ox.ac.uk*
[b] *Faraday Institution, Didcot, UK*
[c] *Australian Nuclear Science and Technology Organisation, Kirrawee, New South Wales, Australia*
[d] *Neutron Scattering Division, Oak Ridge National Laboratory, Oak Ridge, Tennessee, USA*
[e] *Diamond Light Source, Harwell, UK*
[f] *Department of Chemistry, University of Oxford, Oxford, UK*

† Electronic supplementary information (ESI) available. See DOI: https://doi.org/10.1039/d3ee04354a

‡ These authors contributed equally.

Li.[13–16] Despite reaching a composition close to NiO_2 at the end of charge with Ni nominally in the +4 oxidation state, bulk sensitive X-ray absorption spectroscopy (XAS) appears to show incomplete oxidation of Ni^{3+} to Ni^{4+} when the edge position is compared to other Ni^{4+}-containing oxides.[14,15] Some argue that this reflects the change in covalency of the Ni–O bond with the electron–hole density shifting more towards O than Ni when Ni is highly oxidised,[8,17–19] while others argue O oxidation is invoked.[13–15,20]

Recent research into O oxidation in Li-rich cathodes, such as $Li_{1.2}Ni_{0.13}Co_{0.13}Mn_{0.54}O_2$, has indicated that oxidised oxygen takes the form of molecular O_2, which is trapped within vacancy clusters in the cathode structure.[21–25] However, in the case of stoichiometric materials like $LiNiO_2$, it has been argued that this same mechanism cannot apply due to the lack of transition metal vacancies in the fully dense transition metal layers (in the Li-rich materials the Li in the transition metal layers are removed on charge and the remaining vacancies cluster to accommodate the O_2).[14,15]

Here, we perform a structural and spectroscopic study of $LiNiO_2$ on charging to investigate the O-redox mechanism. We employ a combination of neutron and synchrotron X-ray powder diffraction analysis that takes account of the stacking faults prevalent in these charged materials, showing that 8% Ni vacancies form in the originally fully dense transition metal layer as the material is charged across the voltage plateau at 4.2 V *vs.* Li^+/Li. High resolution resonant inelastic X-ray scattering (RIXS) at the O K-edge confirms the presence of trapped molecular O_2, on charging across the 4.2 V *vs.* Li^+/Li plateau, corresponding to approximately 2% of the O in the material. The Ni vacancies result in non-bonding O 2p states on O^{2-} enabling O^{2-} oxidation and 8% Ni vacancies on the transition metal layers is sufficient to form vacancy clusters to accommodate the resulting O_2. Chemical analysis shows that the Ni absent from the bulk does not leave the particles (no Ni was detected in the electrolyte or at the anode after charging). STEM images demonstrate the core–shell nature of the charged particles, with a Ni-rich, $Ni_{1.75}O_2$ rocksalt-like shell approximately 5 nm thick and with a Ni oxidation state of +2.3. The overall Ni oxidation state of the particles charged across the plateau to 4.3 V *vs.* Li^+/Li is determined by Ni L-edge fluorescence yield XAS to be +3.8. However, taking into account the thickness of the shell and its Ni oxidation state of +2.3, the core Ni oxidation state is closer to +4.

Experimental

Materials

Uncoated, polycrystalline $LiNiO_2$ powder was obtained from BASF. The particle morphology is shown on the SEM images in ESI† Fig. S1.

Electrochemistry

Self-supporting cathode films of $LiNiO_2$ were prepared by grinding the material first with acetylene black and then with polytetrafluoroethylene in an 8 : 1 : 1 mass ratio in a pestle and mortar, followed by calendaring to a thickness of ~100 μm. Typical electrodes were 1 cm^2 in size and 15 mg in mass, and the cells were galvanostatically cycled at a rate of 10 mA g^{-1}. Cathodes were assembled into coin cells with 140 μl battery grade 1 M $LiPF_6$ in EC:DMC, 50 : 50 (Merck) used as the electrolyte and Li metal foil as the counter electrode. Cells were disassembled, and the electrodes were rinsed with dry dimethylcarbonate before characterisation. All handling was performed in an MBraun glovebox under inert atmosphere (<1 ppm H_2O and O_2). Electrochemical charge–discharge cycling was carried out using a Maccor Series 4000. For the neutron and X-ray powder diffraction measurements, cathodes with an 8 : 2 ratio of active material to carbon were used and no polytetrafluoroethylene. The cathode was cycled in a custom-made coin cell using a Biologic SP-300 potentiostat. The electrodes had a total mass of 1 g and 50 ml battery grade 1 M $LiPF_6$ in EC:DMC, 50 : 50 (Merck) was used as the electrolyte and Li metal foil as the counter electrode.

Neutron and X-ray powder diffraction

To obtain sufficient neutron power diffraction data, access was obtained from two sources. Time of flight neutron powder diffraction data were obtained from the NOMAD instrument at the Neutron Spallation Source, Oak Ridge National Laboratory.[26] Constant wavelength neutron powder diffraction was measured from the Echidna powder diffractometer[27] at the Australian Center for Neutron Scattering with a wavelength of 1.622 Å. X-ray powder diffraction and total scattering measurements were obtained from XPDF at Diamond Light Source with a wavelength of 0.1616 Å. Instrumental contributions to the peak shapes were obtained through the refinement of Si and LaB_6 standards. In all cases, the samples were sealed under an inert atmosphere within vanadium cans (neutrons) and borosilicate capillaries (X-rays). All measurements were performed at room temperature.

The Rietveld refinements were performed in Topas academic. The background was described by using a combination of a 9th degree Chebyshev polynomial and a scaled scattering pattern of the pure carbon that was used to prepare the electrodes. The X-ray and neutron powder diffraction were refined simultaneously by refining all structural parameters to all detector banks. Each dataset had its individual background and zero error refined. The X-ray and constant wavelength neutron data were modelled using a Thompson-Cox-Hasting pseudo-Voigt profile. The time-of-flight neutron diffraction data were modelled using the instrumental profile of NOMAD implemented in the Topas input file provided by the beamline. The anisotropic peak broadening was modelled using a set of 4 spherical harmonic functions implemented in Topas in the spherical_harmonics_hkl macro.

The pair distribution functions were obtained using PDFgetX3[28] in xPDFsuite[29] and the Pair Distribution Functions were analysed using PDFgui[30] The Rietveld refinements were performed in Topas academic.[31]

STEM

Samples were dispersed in dry dimethylcarbonate (DMC) and transferred onto holey carbon Cu TEM grids by drop-casting inside an argon-filled glovebox and transferred to the microscope using a vacuum transfer holder. ADF-STEM characterisations were obtained using JEOL ARM-200F at the accelerating voltage of 200 kV. The emission current was 5 μA and beam current was 35 pA. A dwell time of 5 μs was used for imaging with a pixel size of 0.006 nm px^{-1}. The inner and outer collecting angles for imaging were 73 and 271 mrad, respectively, with convergence semi-angle of 22.5 mrad.

OEMS

Operando electrochemical mass spectrometry (OEMS) was carried out to detect the evolved gases during galvanostatic charging/discharging of $LiNiO_2$. The setup consists of a quadrupole mass spectrometer (Thermo Fischer) and mass-flow controllers (Bronkhorst). A 2-electrode Swagelok electrochemical cell with gas inlet and outlet ports was used for the *operando* measurements, using $LiNiO_2$ cathode, Li metal anode, Whatman® glass fibre separator, and battery grade 1 M $LiPF_6$ in PC (propylene carbonate) electrolyte. The cells were assembled inside an Ar-filled glovebox. High-purity Ar gas at a flow rate of 1 mL min^{-1} was used as the carrier gas. 1 cm^2 electrodes were used for OEMS with an active cathode material mass loading of 15 mg and cycled at a rate of 10 mA g^{-1}. The OEMS was calibrated for O_2, CO_2 and Ar using standards of known analyte gas content. The carrier gas was Zero Grade Ar (BOC) and the calibration standard was 1011 ppm CO_2 and 1.01% O_2 in Ar base gas (BUSE Scientific). Calibration of the instrument was performed using a dedicated method in the instrument software (GasWorks) which compares the ion flux of analyte gases detected in the instrument with their known concentrations in the calibration standard. Before a current was applied, the cell was flushed using Zero Grade Ar carrier gas until the concentration of Ar measured by the mass spec. was above 99.95%. The baseline CO_2 and O_2 concentrations were then measured for 2 hours before charging the cell.

Spectroscopy

Ni L-edge and O K-edge X-ray absorption spectra and high-resolution O K-edge RIXS were collected at beamline I21 Diamond Light Source.[32] Samples were transferred to the spectrometer using a vacuum-transfer suitcase to avoid air exposure and were pumped down to ultra-high vacuum (UHV) overnight. All measurements were made at a temperature of 20 K to suppress any possible beam damage. RIXS line scans were recorded at the resonance energy for molecular O_2 at 15 different sample locations and averaged together. The acquisition time was 30 seconds for individual RIXS spectra and 1 minute for XAS spectra. To compare the O_2 signal intensity, the areas under the vibrational peaks, excluding the elastic line were integrated between 0.1–2 eV.

ICP

The concentration of Ni in the electrolyte and at the anode was determined through the analysis of inductively coupled plasma-optical emission spectroscopy (ICP-OES) using a Perkin-Elmer Optima 8000 ICP-OES. To prepare the ICP-OES measurements, the cycled coin cells were disassembled and the cathode film and separator in contact with the cathode were discarded. Every other cell part was then left to soak in a diluted aqua reagia solution (Diluted 10 times, giving a 1.2 M concentration of HCl and 1.5 M HNO_3) for 24 hours. The sample solutions were then transferred to the instrument. The ICP-OES was calibrated using a series of diluted standards (200 ppm, 100 ppm, 50 ppm, 10 ppm and 1 ppm) made from an ICP multi-element standard solution IV stock solution obtained from Sigma–Aldrich.

NMR

Magic angle spinning (MAS) ^1H nuclear magnetic resonance (NMR) was carried out at 9.45 T (ν_0 = 400.19 MHz) using a 1.9 mm double air bearing probe (ν_R = 32 kHz) on a Bruker Avance HD spectrometer. A 15-second recycle delay and 512 transients were employed for each experiment using the same rotor.

DFT

Calculations were carried out using the Quantum Espresso (QE) package.[33] As exchange–correlation functional, we employed the generalised gradient approximation (GGA) *via* the Perdew, Burke and Ernzerhof (PBE) functional.[34] The interaction between core and valence electrons was described by using optimised norm-conserving Vanderbilt pseudopotentials (ONCVSP).[35,36] Hubbard corrections to the 3d states of Ni, with U = 6 eV, were included in the calculations (PBE + U), *via* the simplified rotational-invariant formulation of Cococcioni and de Gironcoli. van der Waals (vdW) corrections were also applied, using the Tkatchenko–Scheffler dispersion correction method. The wavefunctions and charge density were represented *via* plane-wave basis sets with energy cutoffs of 120 and 480 Ry, respectively. The energy threshold was set to 1×10^{-8} eV. A $2 \times 2 \times 2$ Monkhorst–Pack k-point grids was employed. Structural models were optimised until forces on the atoms were less than 0.02 eV $Å^{-1}$ and cell stress was less than 0.5 Kbar. To obtain a model for the charged $LiNiO_2$, a model of the pristine material with composition $Li_{0.96}Ni_{1.04}O_2$ was first constructed from a $3 \times 3 \times 1$ supercell of $LiNiO_2$ in the $R\bar{3}m$ space group, containing 26 Li atoms, 28 Ni atoms and 54 O atoms. The lithium was then completed removed and the structure relaxed.

Results and discussion

Structure of $LiNiO_2$ over the first cycle

To investigate the Ni occupancies in the transition metal and Li layers on the first cycle (Fig. 1), a structural investigation was performed using a combination of powder X-ray and neutron diffraction (PXRD and PND). For the study, pristine, undoped and uncoated $LiNiO_2$ was obtained from BASF and handled without exposure to air, see Methods. O K-edge XAS data

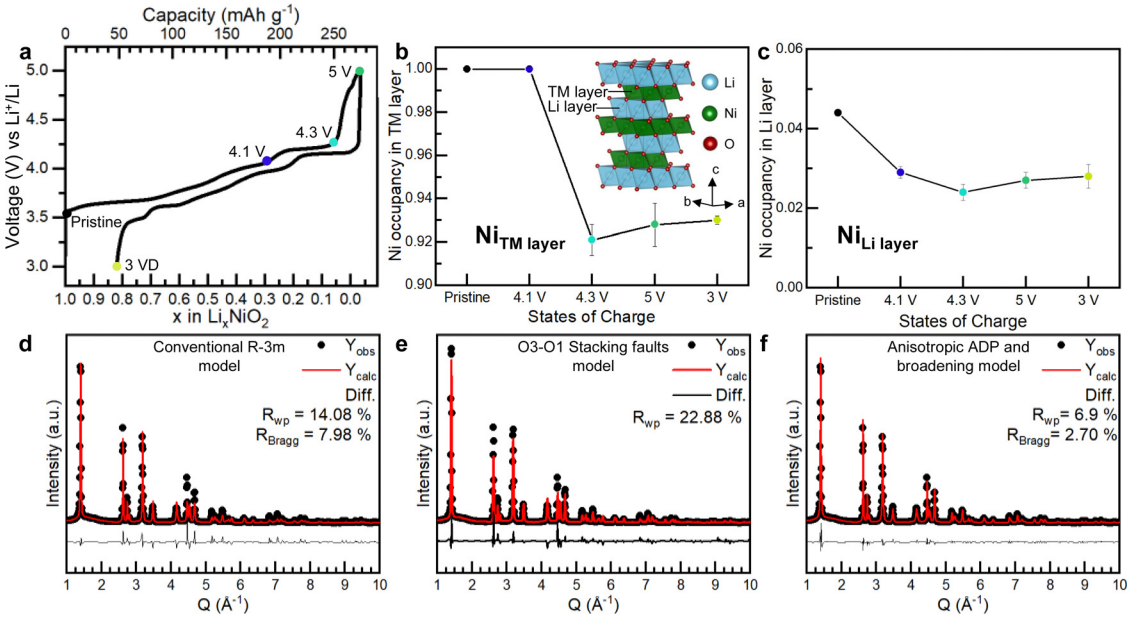

Fig. 1 Electrochemistry and Ni site occupancies for $LiNiO_2$ on the first cycle. (a) First cycle load curve for $LiNiO_2$ (b) and (c) refined site occupancies for Ni in the 3a site (transition metal layer) and 3b site (Li layer) of $LiNiO_2$, respectively, at different states of charge. The line is a guide to the eye. Inset in (b) shows the structure of $LiNiO_2$. (d)–(f) Refinement of the synchrotron PXRD for $LiNiO_2$ charged to 4.3 V *vs.* Li^+/Li using the conventional $R\bar{3}m$ $LiNiO_2$ structure (d), the O3–O1 stacking fault model developed by Croguennec *et al.*[38] refined in Faults[39] (e) and $R\bar{3}m$ $LiNiO_2$ structure, using an anisotropic ADP and peak broadening model (f).

collected in electron and fluorescence yield mode, ESI† Fig. S2, confirm the absence of surface carbonate species which can be observed when $LiNiO_2$ is exposed to air.[37] The refinement of PXRD and PND data reveals that the pristine material is slightly Li deficient with a 4.4% Ni occupancy of the Li 3b site, resulting in the final composition $[Li_{0.956}Ni_{0.044}]NiO_2$. The refinements of the pristine material are shown in ESI† Fig. S3 and Table S1.

$LiNiO_2$ undergoes a series of well-studied phase transitions upon delithiation (H1 → M1 → H2 → H3), between hexagonal phases, H, which differ slightly in their lattice parameters and a monoclinic phase, M.[5,38,40–45] Upon reaching the onset of the voltage plateau at 4.1 V *vs.* Li^+/Li, $LiNiO_2$ has transitioned to the H2 phase with an expanded unit cell along the crystallographic *c* axis, ESI† Fig. S4 and Table S2. At 4.1 V *vs.* Li^+/Li the transition metal layer remains fully dense, Fig. 1b, but the amount of Ni in the Li layer has slightly decreased to 2.9%, Fig. 1c; PXRD and PND refinements at 4.1 V *vs.* Li^+/Li are shown in ESI† Fig. S4 and Table S2. When charging across the voltage plateau and up to 4.3 V *vs.* Li^+/Li, the *c* lattice parameter contracts, ESI† Table S3, in line with previous reports.[5,7,9,10,40,44–46] The simple $R\bar{3}m$ model of the H3 structure at 4.3 V *vs.* Li^+/Li cannot describe the measured diffraction pattern as seen in Fig. 1d. The discrepancy between the model and the data could stem from the formation of O1 stacking faults as previously reported.[38,39,47] At 4.3 V *vs.* Li^+/Li and above, there is little to no Li in the structure, and since we are primarily interested in the Ni behaviour we focused on the PXRD data here as this is most sensitive to the Ni.

O1-type stacking faults in delithiated $LiNiO_2$ have previously been modelled by introducing O1 layers of a well-defined interlayer spacing and a displacement vector into the O3 structure using DIFFaX and Faults software.[38,39] However, as shown in Fig. 1e, this model does not adequately describe the diffraction pattern at 4.3 V *vs.* Li^+/Li. As shown in Fig. 1d and e and in ESI† Fig. S5 both the regular $R\bar{3}m$ model and the O1 stacking fault model cannot describe the intensity and the shape of the Bragg peaks. Instead, we find that using anisotropic atomic displacement parameters (ADP) and taking into account the anisotropic peak broadening by using a set of spherical harmonics substantially improves the refinement, as shown in Fig. 1f and ESI† Fig. S5. This implies that the interlayer distances are more variable than can be accounted for by a binary stacking model.

Using this model, which accurately describes the *hkl*-dependent peak broadening, the Ni occupancy in the 3a sites in the transition layer was refined. The refinements, which are summarised in Fig. 1f, ESI† Fig. S4 and S5 and Tables S3 and S4, show that the Ni occupancy decreases to around 92–93% in both the 4.3 V *vs.* Li^+/Li and 5 V *vs.* Li^+/Li samples, Fig. 1b. Moreover, joint Rietveld refinements of neutron and X-ray scattering data of the discharged $LiNiO_2$, which does not contain stacking faults, also show there are 8% vacancies in the transition metal layer (ESI† Fig. S7 and Table S5). These results show that the transition metal layer does not remain fully dense on charging across the voltage plateau and that the vacant Ni sites are not repopulated with Ni during the discharge process.

To investigate if the Ni migrates to the Li layer, the Ni occupancy in the 3b sites in the Li layer was refined. As shown in Fig. 1c, the amount of Ni in the Li layers remains constant at

about 2–3% across the voltage plateau and on discharge. Refinements were also performed by introducing Ni into tetrahedral interstices in the structure, but this did not improve the fit, ESI† Fig. S8. The refinements, therefore, show that on charging up to and across the 4.2 V *vs.* Li^+/Li plateau, 8% of the Ni is lost from the bulk, corresponding to a composition change from $[Li_{0.956}Ni_{0.044}]NiO_2$ in the pristine material to $[Li_0Ni_{0.028}]Ni_{0.926}O_2$ at 5 V *vs.* Li^+/Li and that these Ni occupancies remain on discharge to 3 V *vs.* Li^+/Li.

To determine the destination of the Ni lost from the bulk, the electrolyte along with the solution after dissolving the anode were analysed by Inductively coupled plasma optical emission spectrometry (ICP-OES). The ICP-OES results are presented in ESI† Table S6 and show that only negligible amounts of Ni (147 ppm, which corresponds to 0.3 mmol of Ni loss per mole of cathode) leave the cathode material on charging. These results suggest that the Ni from the bulk remains in the particles and likely accumulates in the near-surface region of the particles, resulting in a core–shell structure.

Local structure of $LiNiO_2$ on charging and surface shell composition

Densification at the cathode particle surface to form a rocksalt-like layer at high degrees of delithiation is a well-studied phenomenon in $LiNiO_2$. This is generally related to O-loss which reduces the O content at the surface and triggers Ni migration inward to sites in the Li layer.[5,24,48–53] To quantify O-loss in our sample, operando electrochemical mass spectrometry (OEMS) was performed for $LiNiO_2$ over the first cycle, ESI† Fig. S9 and S10. While no direct O_2 evolution was observed throughout the charging/discharging, some CO_2 is released, starting at the onset of the voltage plateau. The CO_2 arises from an attack of oxidised oxygen species from the cathode lattice on the carbonate solvents in the electrolyte and can be used to quantify the amount of oxygen released from the surface, as previously demonstrated.[8,21,54–60] The quantity of CO_2 released during charge up to 4.7 V *vs.* Li^+/Li is 0.89 mmol $g^{-1}{}_{(LNO)}{}^{-1}$, indicating that up to 0.04 moles of O are lost per mole of $LiNiO_2$, see Methods.

To examine the growth and thickness of the densified layer with state of charge, annular dark field scanning transmission electron microscopy (ADF-STEM) was performed. The morphology of the material is composed of the typical primary/secondary particle agglomerates, see SEM in ESI† Fig. S1. These were sonicated to release the primary particles for STEM analysis. The images are shown in Fig. 2a–l. The high-resolution images in Fig. 2e–h, show the evolution of the surface structure. The layered structure at the surface of the pristine material, Fig. 2e, gives way to the beginning of a cation-mixed, rocksalt-like surface at 4.1 V *vs.* Li^+/Li, evident from the appearance of scattering intensity from the Li layers due to the presence of Ni Fig. 2f. The emergence of this rocksalt-like surface at 4.1 V *vs.* Li^+/Li is in line with the observed small amount of O-loss at the onset of the voltage plateau, ESI† Fig. S8. To determine the thickness of this surface layer, the variations in scattering intensity along three atom rows, i, ii and iii, from the surface to the bulk, Fig. 2e–h, were examined. The intensity of the three lines was averaged and is shown in Fig. 2m–p. The intensities are dominated by the scattering from Ni and show where there are regions of high and low Ni content. The more intense peaks arise from Ni in transition metal layers, and the weaker peaks from Ni in the Li layers. The ratios of the intensity maxima of the high and low-intensity peaks are plotted as the red line in Fig. 2n to p. On moving from bulk to surface, the variation in scattering intensity diminishes in accord with moving from a layered to a rocksalt-like distribution of Ni ions. The transition from layered to rocksalt-like structure does not occur abruptly but has a small transition region. However, the region where the rocksalt dominates appears initially with a thickness of around 1 nm at 4.1 V *vs.* Li^+/Li, Fig. 2n, and grows to around 5 nm by 4.7 V *vs.* Li^+/Li, Fig. 2p.

Considering the images taken from the bulk of the particles (Fig. 2i–l), the layered ordering is maintained throughout the charge, Fig. 2i–l. Intensity analysis was carried out within the blue-shaded regions in Fig. 2i–l. Intensities were integrated along the transition and Li layers, respectively and then plotted across the layers, Fig. 2q. They confirm the retention of the layered structure in the bulk. Between 4.1 V *vs.* Li^+/Li and 4.3 V *vs.* Li^+/Li, the interlayer spacing contracts slightly in agreement with the diffraction results.

Given an average primary particle size of 250 nm as seen in STEM and SEM, ESI† Fig. S1, and a shell thickness of 5 nm, as observed by STEM, Fig. 2h and p, and assuming spherical particles, consistent with the approximately primary particle morphology, seen in ESI† Fig. S1, the rocksalt shell occupies approximately 12% of the volume of the cathode. The 0.04 moles of surface O-loss results in an increase of 0.02 moles of Ni in the densified layer. This, in addition to the 0.08 moles of Ni from the bulk to the surface, yields a shell composition of $Ni_{1.75}O_2$ and, therefore an overall Ni oxidation state of +2.3.

Ni *versus* O oxidation in $LiNiO_2$

To probe the extent of Ni oxidation in $LiNiO_2$ on charging, Ni L-edge XAS was performed in bulk sensitive fluorescence yield (FY) mode (approximately 50–100 nm penetration depth, *i.e.* depth of the primary particles). The obtained spectra for $LiNiO_2$ at different states of charge over the first cycle are displayed in Fig. 3a. The pristine spectrum closely resembles other measurements taken on $LiNiO_2$ indicating an initial oxidation state of close to Ni^{3+}.[13] On charging, the edge shape changes are consistent with Ni oxidising towards +4. Ni oxidation continues across the voltage plateau at 4.215 V; as seen in the reduction in intensity of the peak at 853 eV, Fig. 3a. Beyond 4.3 V *vs.* Li^+/Li, the L-edge spectra show little further change. It is important to note that the plateau is associated with a two-phase reaction, and the data suggests that the Ni oxidation state is higher in the composition at 4.3 V *vs.* Li^+/Li than in the composition at 4.1 V *vs.* Li^+/Li at the beginning of the plateau. It does not imply a continuous evolution of Ni oxidation state as would be the case for a solid solution. The fact that the spectra for the 4.3 V *vs.* Li^+/Li and 5.0 V *vs.* Li^+/Li samples still exhibit the 853 eV shoulder

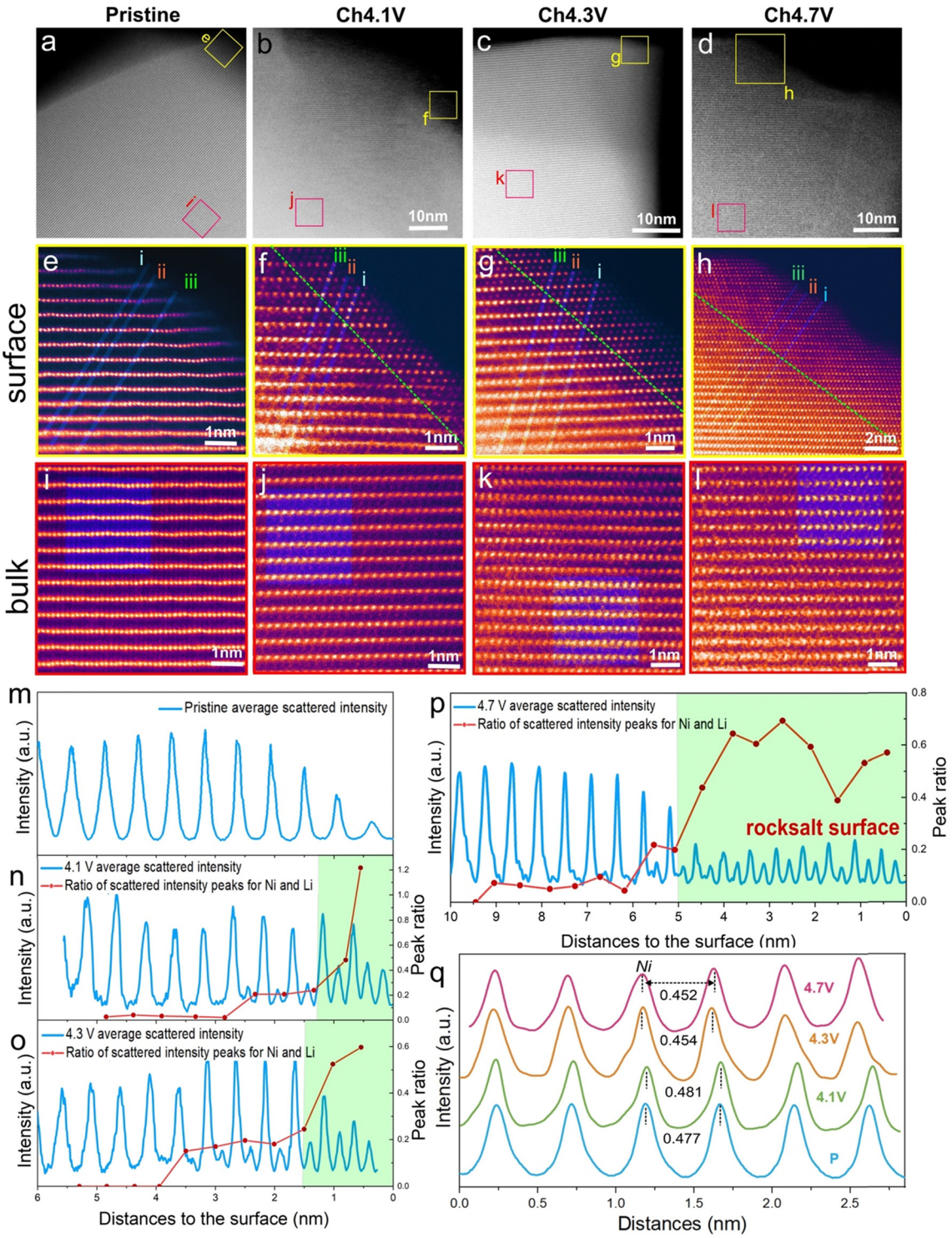

Fig. 2 Surface and bulk ADF-STEM images for $LiNiO_2$ on the first charge. (a)–(d) Wide field of view ADF-STEM images for $LiNiO_2$ at increasing states of charge on the first cycle with the surface (yellow boxes) and bulk (red boxes) regions highlighted and examined in closer detail (e)–(h) and (i)–(l), respectively. (e)–(h) ADF-STEM images from the $LiNiO_2$ surface at each state of charge. A shell (surface layer) with a mixing of Ni between the transition and Li layers grows in thickness on charge from 4.1 V *vs.* Li^+/Li. The shell is bound by the green dotted line. The thickness of the evolving shell and therefore position of the green dotted line is established from the data in Fig. 2m to p. (i)–(l) ADF-STEM images of the $LiNiO_2$ bulk regions taken about 50 nm away from the surface at each state of charge showing preservation of the layered structure. (m)–(p) Variation in scattering intensity from the surface to the bulk was obtained by averaging the three numbered line scans in (e)–(h). The ratios of the intensity maxima of the Ni_{Li} peak (Ni in the lithium metal layer) to the Ni_{Ni} peak (Ni in the transition metal layer) are plotted as the red line in the figures. It shows the transition from a rocksalt-like structure (where the Ni occupancies in the Li and transition metal layers are closer) to a layered structure (where they are different). (q) Within the bulk of the particles, Fig. 2(i) to (l), scattering intensities are integrated along the transition metal and Li layers, respectively, within the green-shaded regions, then plotted across the layers. They confirm the layered structure is retained in the bulk on charging.

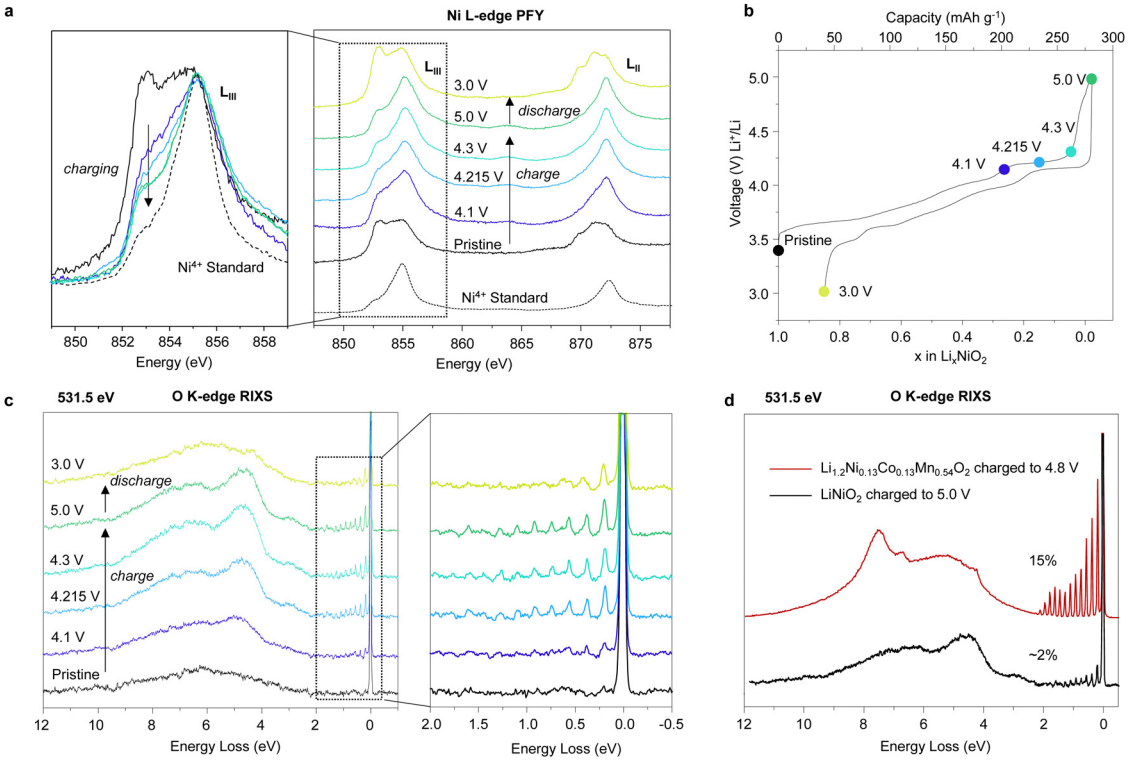

Fig. 3 Spectroscopy of $LiNiO_2$ on the first cycle. (a) Ni L-edge X-ray absorption spectra for $LiNiO_2$ at different states of charge over the first cycle, colours correspond to points in (c). $Li_{1.2}Ni_{0.13}Co_{0.13}Mn_{0.54}O_2$ charged to a lithium content of 0.8 is used as a standard reference for Ni^{4+}. Ni L_{III}-edge spectra show continuous peak intensity reduction at 853 eV, indicating oxidation of Ni across the voltage plateau between 4.1 V *vs.* Li^+/Li and 4.3 V *vs.* Li^+/Li. (b) First cycle load curve for $LiNiO_2$. (c) High-resolution O K-edge RIXS for $LiNiO_2$ measured at the resonance energy for molecular O_2. The vibrational peaks between 0 eV and 2 eV energy loss indicate the formation of trapped molecular O_2 across the voltage plateau. (d) Comparison of the signal intensity of the vibrational peaks arising from O_2 between $LiNiO_2$ charged to 5 V *vs.* Li^+/Li and $Li_{1.2}Ni_{0.13}Co_{0.13}Mn_{0.54}O_2$ are consistent with about 2% of the O in $LiNiO_2$ in the form of molecular O_2. The amount of O_2 in $Li_{1.2}Ni_{0.13}Co_{0.13}Mn_{0.54}O_2$ is approximately 15%.

peak is consistent with an overall Ni oxidation state being less than +4. Comparing the data with the Ni L-edge spectrum of a Ni^{4+} reference material, $Li_{0.8}Ni_{0.13}Co_{0.13}Mn_{0.54}O_2$, indicates that the overall Ni oxidation state for the particles charged to 4.3 V *vs.* Li^+/Li and beyond is approximately +3.8

While fluorescence yield XAS probes to a depth of 50–100 nm, the signal inevitably contains a contribution from the surface. Electron yield data with a probe depth of around 10–20 nm, ESI† Fig. S11, confirm that the surface Ni is more reduced than that obtained from fluorescence mode, as indicated by a sharp, distinct peak at 853 eV consistent with the 5 nm thick $Ni^{2.3+}$ shell discussed above. Given that the fluorescence mode contains a contribution of $Ni^{2.3+}$ from the shell at the surface and that the Ni L-edge fluorescence yield indicates an overall oxidation state of $Ni^{3.8+}$ the results from the two modes suggest the Ni in the core is closer to +4.

At the end of charge, all of the 0.96 mol of Li have been removed from $LiNiO_2$ ($Li_{0.96}Ni_{0.04}[Ni]O_2$). Given the shell is +2.3, the bulk is closer to +4 and the overall particle Ni oxidation state is approximately +3.8, which is consistent with the XAS spectrum at 5.0 V *vs.* Li^+/Li, approximately 0.16 mol of electrons must arise from O oxidation. Our quantitative OEMS have already shown that surface O-loss accounts for 0.08 mol of lithium extraction (0.04 mol of O lost). We can, therefore, assign the remaining 0.08 mol to bulk oxygen oxidation.

To investigate the bulk O-redox mechanism, O K-edge RIXS measurements were obtained. Previous RIXS measurements on Li-rich cathodes have revealed that O oxidation results in the formation of O_2 molecules trapped within the cathode particles.[21–23,25,61–63] The RIXS measurements for $LiNiO_2$ (Fig. 3c and d), also show the same vibrational features at an excitation energy of 531.5 eV as those previously attributed to O_2, Fig. 3c. The features begin to appear at the onset of the voltage plateau and increase in intensity up to the end of charge. On discharge to 3 V *vs.* Li^+/Li, only a small quantity of O_2 remains, indicating an almost complete reduction of O_2 back to O^{2-}.

By comparing the area under the signal to RIXS spectra obtained under the same measurement conditions for charged $Li_{1.2}Ni_{0.13}Co_{0.13}Mn_{0.54}O_2$, where the amount of O_2 is known, it is possible to estimate approximately how much O_2 is present in the $LiNiO_2$ charged to 5 V *vs.* Li^+/Li, see the Methods section and ESI† Fig. S12. The results displayed in Fig. 3d suggest that 2% of the O in $LiNiO_2$ charged to 5 V *vs.* Li^+/Li is in the form of trapped molecular O_2, Fig. 3d, corresponding to 0.08 moles of Li extraction (20 mA h g^{-1}), in good accord with the amount

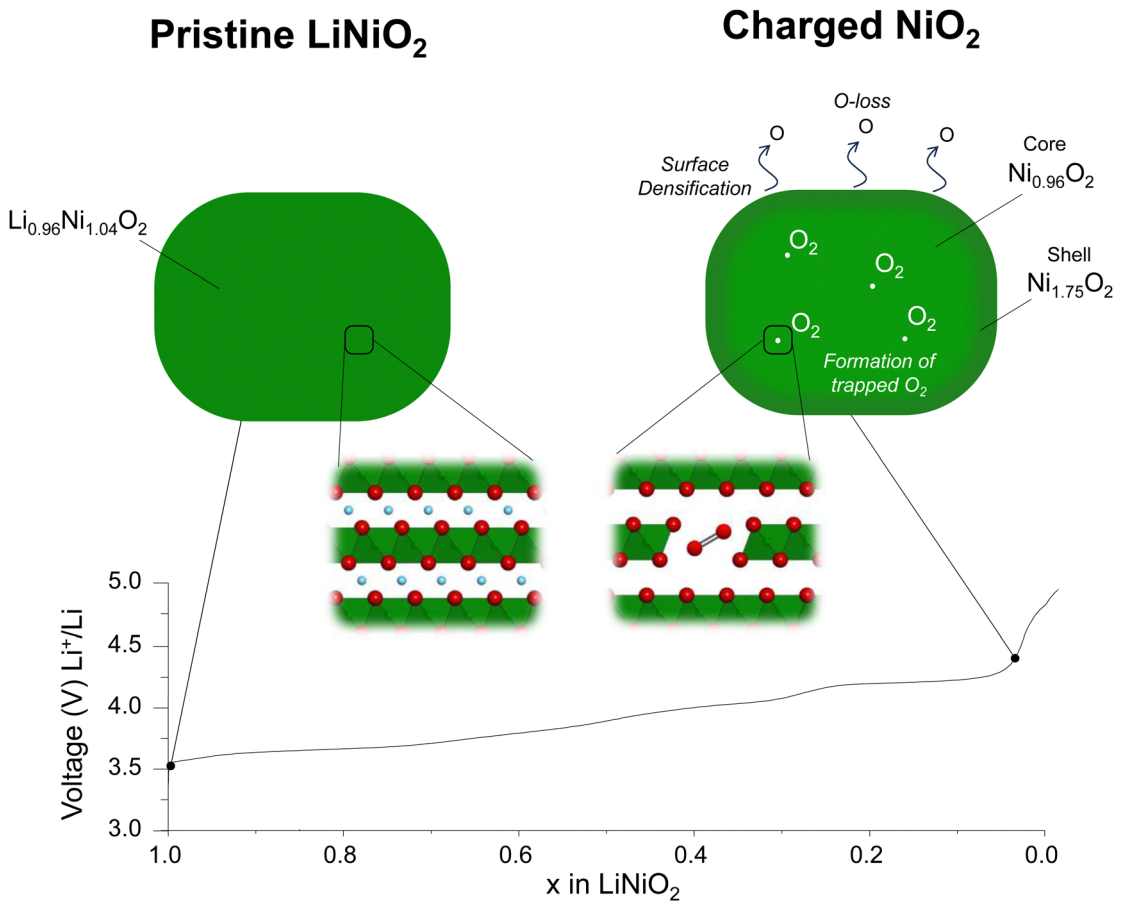

Fig. 4 Schematic of charging mechanisms in $LiNiO_2$. Ni vacancies are formed in the transition metal layer on charging across the 4.2 V *vs.* Li^+/Li plateau, generating non-bonded O 2p states that activate O^{2-} oxidation and enabling Ni rearrangement into vacancy clusters that can accommodate trapped O_2 molecules.

of O-oxidation implied from the overall Ni oxidation state. This amount of O_2 could feasibly be accommodated by the 8% Ni vacancies in the transition metal layer observed in the charged cathode, if each O_2 molecule is trapped within a cluster of four vacancies, as proposed previously.[21,23,25,62,64,65]

In previous studies of lithium rich materials such as $Li[Li_{0.2}Ni_{0.13}Co_{0.13}Mn_{0.54}]O_2$, we have shown using density functional theory (DFT) how vacancy clusters form in the transition metal layers through metal migration, permitting the formation of trapped O_2.[21,64] Total energy calculations show that structures containing trapped O_2 are substantially lower in energy than other configurations of the charged structure by as much as 410 meV f.u.$^{-1}$, indicating a thermodynamic driving force behind trapped O_2 formation. To demonstrate that $LiNiO_2$ behaves in a consistent manner with our previously investigated systems, we computed the energy difference for charged $LiNiO_2$ before and after the formation of vacancy clusters and trapped O_2. The calculations (ESI† Fig. S14 and Table S7) show that the structure with O_2 is 205 meV f.u.$^{-1}$ lower in energy than the structure without, in line with our earlier work.

Close inspection of the relaxed structural model with trapped O_2 molecules shows an O–O bond length of 1.2 Å, close to that of free O_2, indicating there is little evidence for a strong coordination interaction with the neighbouring Ni. This accords with our previous modelling for Mn-based transition metal oxides, and experimental vibrational RIXS data for the 4d and 5d-TM systems.[66]

Discussion

Unlike Li-rich layered oxides, Li^+ extraction from stoichiometric Ni-rich cathodes could in principle be charge compensated by transition metal oxidation alone. It has further been argued that, due to the lack of cation vacancies in the transition metal layers and the absence of non-bonding O 2p orbitals, O-redox, oxidation of O^{2-} ions, as observed in Li-rich cathodes does not apply to the Ni-rich systems.[14,15]

Our results reveal that the structural instability in the bulk of $LiNiO_2$ is more extensive than previously thought. On oxidation of $[Li_{0.956}Ni_{0.044}]NiO_2$, Li^+ extraction is charge compensated by oxidation of Ni +2.96 to +3.63 at the onset of the 4.2 V *vs.* Li^+/Li plateau. On charging across and beyond the plateau, O^{2-} ions are oxidised, resulting in oxygen loss at the surface and the growth of a Ni-rich surface layer reaching approximately 5 nm thick. In the bulk, O^{2-} oxidation forms O_2 trapped in the

particles. This is enabled by the loss of Ni from the transition metal layers forming 8% Ni vacancies. Ni vacancies on the transition metal sites have two consequences: they generate non-bonding O 2p orbitals activating O^{2-} oxidation and they enable Ni reorganisation and vacancy clustering necessary to accommodate the O_2 molecules, explaining how it is possible to form trapped O_2 in stoichiometric compounds that do not initially have Li^+ or vacancies in the transition metal layers. The Ni no longer present in the bulk is not lost from the particles, instead forming part of a Ni-rich shell with a composition of $Ni_{1.75}O_2$.[23,61,62] The overall Ni oxidation state of the particles as determined by Ni L edge XAS in fluorescence yield, *i.e.* bulk mode, and the oxygen RIXS data show respectively that Ni and O^{2-} are oxidised on charing across the 4.2 V *vs.* Li^+/Li plateau. However, the plateau is associated with a two-phase reaction and all we can conclude is that the phase at the charged end of the plateau at 4.3 V *vs.* Li^+/Li contains Ni in a higher oxidation state than before the plateau and that O-redox has occurred. It does not imply that O-redox commences before Ni is oxidised to +4. The bulk fluorescence yield mode gives the overall Ni oxidation state for the charged particles as +3.8. However, it includes the shell, which has a Ni oxidation state of +2.3 and grows across the plateau. The implication is that the Ni oxidation state in the core of the core–shell particles is very close to +4 from 4.3 V *vs.* Li^+/Li onwards. Therefore, we do not see evidence of O-redox commencing before Ni is oxidised to +4.

O K-edge RIXS data were recently reported by Piper and co-workers[15] on $LiNi_{0.98}W_{0.02}O_2$ showing a series of sharp peaks in the emission spectrum between 0–2 eV energy loss at the top of charge.[15] While the authors acknowledged that these features were identical to those attributed to molecular O_2 in Li-rich cathodes, they argued that since they could not observe vacant Ni sites in the transition metal layer of the charged cathode, there was no possibility of vacancy cluster formation to accommodate O_2 in the Ni-rich materials. Instead, Morris and co-workers[14] proposed that O–O dimers form by a water-assisted decomposition of oxidised lattice O and they are not intrinsic to the O-redox mechanism.[14] According to their model, H_2O and OH groups should be present in the empty Li layer. However, ^1H magic angle spinning (MAS) NMR data collected on our $LiNiO_2$ sample charged to 5 V *vs.* Li^+/Li do not detect protons, ESI† Fig. S15. In contrast, our results identifying the presence of Ni vacancies in the transition metal layer, suggest that the trapped O_2 can arise through a similar process of O^{2-} oxidation to that observed in the Li-rich layered cathodes. The results are summarised in the schematic in Fig. 4.

Conclusion

A combined powder neutron and X-ray diffraction study, taking account of random stacking faults, revealed that charging $LiNiO_2$ across the plateau at 4.2 V *vs.* Li^+/Li induces the formation of Ni vacancies in the previously fully dense transition metal layers in the bulk of the cathode. These vacant sites have two consequences: they activate the oxidation of O^{2-} by forming non-bonding O 2p orbitals and the observed 8% of Ni vacancies are sufficient to form vacancy clusters able to accommodate trapped molecular O_2 formed on O^{2-} oxidation which we observe by high-resolution RIXS, similar to the mechanism of O-redox observed in Li-rich cathodes. Beyond the 4.2 V *vs.* Li^+/Li plateau, the particles exhibit a core–shell morphology with a $Ni_{1.75}O_2$ shell and a Ni oxidation state of +2.3, while the core has a Ni oxidation state close to +4. Together, the results reveal that although charging is predominantly associated with Ni oxidation, the bulk structure of delithiated $LiNiO_2$ is liable to changes on charging to accommodate trapped molecular O_2. Our study shows the mechanism of O-redox involving the formation of trapped O_2 in the bulk is general to both Li-rich materials and $LiNiO_2$ despite the latter possessing fully dense transition metal layers in the pristine state.

Author contributions

Mikkel Juelsholt, Jun Chen, Robert A. House, and Peter G. Bruce conceived the project and wrote the manuscript with contributions from all authors. Mikkel Juelsholt and Miguel A. Pérez-Osorio performed the structural analysis of the diffraction data in close collaboration with Helen E. Maynard-Casely, Jue Liu and Michelle Everett. Jun Chen did the STEM measurements and performed their analysis together with Rob A House and Mikkel Juelsholt. Sofia De Sousa Coutinho and Mikkel Juelsholt measured and analysed the ICP. Gregory J. Rees performed and analysed the MAS NMR experiments. Robert A. House, working closely with Stefano Agrestini, Mirian Garcia-Fernandez and Ke-Jin Zhou conducted, processed and interpreted the RIXS and soft XAS measurements. Robert A. House and Peter G. Bruce supervised the project. Miguel A. Pérez-Osorio performed the DFT calculations.

Conflicts of interest

The authors declare that there are no conflicts of interest.

Acknowledgements

We are indebted to the Engineering and Physical Sciences Research Council (EPSRC), the Henry Royce Institute for Advanced Materials (EP/R00661X/1, EP/S019367/1, EP/R010145/1, EP/L019469/1) and the Faraday Institution (FIRG007, FIRG008, FIRG016) for financial support. We acknowledge Diamond Light Source for time on Beamlines I15-1 XPDF and I21 under Proposals MM27764-1 and MM29028-1. We thank the Spallation Neutron Source, a Department of Energy Office of Science User Facility operated by the Oak Ridge National Laboratory, for providing neutron powder diffraction measurements. We acknowledge the support of the Australian Centre for Neutron Scattering, ANSTO and the Australian Government through the National Collaborative Research Infrastructure Strategy in supporting the neutron research infrastructure used in this work *via* ACNS proposal

MI13571. This project was supported by the Royal Academy of Engineering under the Research Fellowship scheme. We also acknowledge the resources provided by the Cambridge Tier-2 system operated by the University of Cambridge Research Computing Service (https://www.hpc.cam.ac.uk) funded by EPSRC Tier-2 capital grant EP/P020259/1, *via* the BATTSurface, NextCATHODE and SOLEL projects. For the purpose of Open Access, the author has applied a CC BY public copyright licence to any Author Accepted Manuscript version arising from this submission.

References

1 S.-T. Myung, F. Maglia, K.-J. Park, C. S. Yoon, P. Lamp, S.-J. Kim and Y.-K. Sun, *ACS Energy Lett.*, 2017, **2**, 196–223.
2 F. Schipper, E. M. Erickson, C. Erk, J.-Y. Shin, F. F. Chesneau and D. Aurbach, *J. Electrochem. Soc.*, 2017, **164**, A6220.
3 J. Xu, F. Lin, M. M. Doeff and W. Tong, *J. Mater. Chem. A*, 2017, **5**, 874–901.
4 S. G. Booth, A. J. Nedoma, N. N. Anthonisamy, P. J. Baker, R. Boston, H. Bronstein, S. J. Clarke, E. J. Cussen, V. Daramalla, M. De Volder, S. E. Dutton, V. Falkowski, N. A. Fleck, H. S. Geddes, N. Gollapally, A. L. Goodwin, J. M. Griffin, A. R. Haworth, M. A. Hayward, S. Hull, B. J. Inkson, B. J. Johnston, Z. Lu, J. L. MacManus-Driscoll, X. Martínez De Irujo Labalde, I. McClelland, K. McCombie, B. Murdock, D. Nayak, S. Park, G. E. Pérez, C. J. Pickard, L. F. J. Piper, H. Y. Playford, S. Price, D. O. Scanlon, J. C. Stallard, N. Tapia-Ruiz, A. R. West, L. Wheatcroft, M. Wilson, L. Zhang, X. Zhi, B. Zhu and S. A. Cussen, *APL Mater.*, 2021, **9**, 109201.
5 M. Bianchini, M. Roca-Ayats, P. Hartmann, T. Brezesinski and J. Janek, *Angew. Chem.,Int. Ed.*, 2019, **58**, 10434–10458.
6 C. S. Yoon, D. W. Jun, S. T. Myung and Y. K. Sun, *ACS Energy Lett.*, 2017, **2**, 1150–1155.
7 L. de Biasi, A. Schiele, M. Roca-Ayats, G. Garcia, T. Brezesinski, P. Hartmann and J. Janek, *ChemSusChem*, 2019, **12**, 2240–2250.
8 F. Kong, C. Liang, L. Wang, Y. Zheng, S. Perananthan, R. C. Longo, J. P. Ferraris, M. Kim and K. Cho, *Adv. Energy Mater.*, 2019, **9**, 1802586.
9 C. Xu, P. J. Reeves, Q. Jacquet and C. P. Grey, *Adv. Energy Mater.*, 2021, **11**, 2003404.
10 H. Li, N. Zhang, J. Li and J. R. Dahn, *J. Electrochem. Soc.*, 2018, **165**, A2985.
11 E. Levi, M. D. Levi, G. Salitra, D. Aurbach, R. Oesten, U. Heider and L. Heider, *Solid State Ionics*, 1999, **126**, 97–108.
12 H. Nguyen, R. Silverstein, A. Zaveri, W. Cui, P. Kurzhals, S. Sicolo, M. Bianchini, K. Seidel and R. J. Clément, *Adv. Funct. Mater.*, 2023, 2306168.
13 N. Li, S. Sallis, J. K. Papp, J. Wei, B. D. McCloskey, W. Yang and W. Tong, *ACS Energy Lett.*, 2019, **4**, 2836–2842.
14 A. R. Genreith-Schriever, H. Banerjee, A. S. Menon, E. N. Bassey, L. F. J. Piper, C. P. Grey and A. J. Morris, *Joule*, 2023, **7**, 1623–1640.
15 A. S. Menon, B. J. Johnston, S. G. Booth, L. Zhang, K. Kress, B. E. Murdock, G. Paez Fajardo, N. N. Anthonisamy, N. Tapia-Ruiz, S. Agrestini, M. Garcia-Fernandez, K. Zhou, P. K. Thakur, T. L. Lee, A. J. Nedoma, S. A. Cussen and L. F. J. Piper, *PRX Energy*, 2023, **2**, 13005.
16 P. Kurzhals, F. Riewald, M. Bianchini, H. Sommer, H. A. Gasteiger and J. Janek, *J. Electrochem. Soc.*, 2021, **168**, 110518.
17 Dm. M. Korotin, D. Novoselov and V. I. Anisimov, *Phys Rev B*, 2019, **99**, 45106.
18 K. Foyevtsova, I. Elfimov, J. Rottler and G. A. Sawatzky, *Phys Rev B*, 2019, **100**, 165104.
19 D. A. Kitchaev, J. Vinckeviciute and A. Van Der Ven, *J. Am. Chem. Soc.*, 2021, **143**, 1908–1916.
20 N. Li, S. Sallis, J. K. Papp, B. D. McCloskey, W. Yang and W. Tong, *Nano Energy*, 2020, **78**, 105365.
21 R. A. House, J. J. Marie, M. A. Pérez-Osorio, G. J. Rees, E. Boivin and P. G. Bruce, *Nat. Energy*, 2021, **6**, 781–789.
22 R. Sharpe, R. A. House, M. J. Clarke, D. Förstermann, J.-J. Marie, G. Cibin, K.-J. Zhou, H. Y. Playford, P. G. Bruce and M. S. Islam, *J. Am. Chem. Soc.*, 2020, **142**, 21799–21809.
23 R. A. House, G. J. Rees, K. McColl, J.-J. Marie, M. Garcia-Fernandez, A. Nag, K.-J. Zhou, S. Cassidy, B. J. Morgan, M. Saiful Islam and P. G. Bruce, *Nat. Energy*, 2023, **8**, 351–360.
24 J. Feng, Z. Chen, W. Zhou and Z. Hao, *Mater. Horiz.*, 2023, **10**, 4686–4709.
25 R. A. House, H. Y. Playford, R. I. Smith, J. Holter, I. Griffiths, K.-J. Zhou and P. G. Bruce, *Energy Environ. Sci.*, 2022, **15**, 376–383.
26 J. Neuefeind, M. Feygenson, J. Carruth, R. Hoffmann and K. K. Chipley, *Nucl. Instrum. Methods Phys. Res., Sect. B*, 2012, **287**, 68–75.
27 M. Avdeev and J. R. Hester, *J. Appl. Crystallogr.*, 2018, **51**, 1597–1604.
28 P. Juhás, T. Davis, C.-L. Farrow and S.-J.-L. Billinge, *J. Appl. Crystallogr.*, 2013, **46**, 560–566.
29 X. Yang, P. Juhás, C. L. Farrow and S. J. L. Billinge, arXiv: Materials Science.
30 C. L. Farrow, P. Juhas, J. W. Liu, D. Bryndin, E. S. Božin, J. Bloch, T. Proffen and S. J. L. Billinge, *J. Phys.: Condens. Matter*, 2007, **19**, 335219.
31 A. A. Coelho, *J. Appl. Crystallogr.*, 2018, **51**, 210–218.
32 K.-J. Zhou, A. Walters, M. Garcia-Fernandez, T. Rice, M. Hand, A. Nag, J. Li, S. Agrestini, P. Garland, H. Wang, S. Alcock, I. Nistea, B. Nutter, N. Rubies, G. Knap, M. Gaughran, F. Yuan, P. Chang, J. Emmins and G. Howell, *J. Synchrotron Radiat.*, 2022, **29**, 563–580.
33 P. Giannozzi, S. Baroni, N. Bonini, M. Calandra, R. Car, C. Cavazzoni, D. Ceresoli, G. L. Chiarotti, M. Cococcioni, I. Dabo, A. Dal Corso, S. de Gironcoli, S. Fabris, G. Fratesi, R. Gebauer, U. Gerstmann, C. Gougoussis, A. Kokalj, M. Lazzeri, L. Martin-Samos, N. Marzari, F. Mauri, R. Mazzarello, S. Paolini, A. Pasquarello, L. Paulatto, C. Sbraccia, S. Scandolo, G. Sclauzero, A. P. Seitsonen, A. Smogunov, P. Umari and R. M. Wentzcovitch, *J. Phys.: Condens. Matter*, 2009, **21**, 395502.

34 J. P. Perdew, K. Burke and M. Ernzerhof, *Phys. Rev. Lett.*, 1996, **77**, 3865–3868.
35 M. Schlipf and F. Gygi, *Comput. Phys. Commun.*, 2015, **196**, 36–44.
36 D. R. Hamann, *Phys Rev B: Condens. Matter Mater. Phys.*, 2013, **88**, 85117.
37 R. J. Green, H. Wadati, T. Z. Regier, A. J. Achkar, C. McMahon, J. P. Clancy, H. A. Dabkowska, B. D. Gaulin, G. A. Sawatzky and D. G. Hawthorn, 2020.
38 L. Croguennec, C. Pouillerie, A. N. Mansour and C. Delmas, *J. Mater. Chem.*, 2001, **11**, 131–141.
39 M. Casas-Cabanas, M. Reynaud, J. Rikarte, P. Horbach and J. Rodriguez-Carvajal, *J. Appl. Crystallogr.*, 2016, **49**, 2259–2269.
40 J. Molenda, P. Wilk and J. Marzec, *Solid State Ionics*, 2002, **146**, 73–79.
41 L. Croguennec, C. Pouillerie and C. Delmas, *Solid State Ionics*, 2000, **135**, 259–266.
42 C. Delmas, J. P. Pérès, A. Rougier, A. Demourgues, F. Weill, A. Chadwick, M. Broussely, F. Perton, Ph Biensan and P. Willmann, *J. Power Sources*, 1997, **68**, 120–125.
43 J. C. Garcia, J. Gabriel, N. H. Paulson, J. Low, M. Stan and H. Iddir, *J. Phys. Chem. C*, 2021, **125**, 27130–27139.
44 P.-H. Chien, X. Wu, B. Song, Z. Yang, C. K. Waters, M. S. Everett, F. Lin, Z. Du and J. Liu, *Batteries Supercaps*, 2021, **4**, 1701–1707.
45 W. Li, J. N. Reimers and J. R. Dahn, *Solid State Ionics*, 1993, **67**, 123–130.
46 E. Bautista Quisbert, F. Fauth, A. M. Abakumov, M. Blangero, M. Guignard and C. Delmas, *Small*, 2023, **19**, 2300616.
47 K.-Y. Park, Y. Zhu, C. G. Torres-Castanedo, H. J. Jung, N. S. Luu, O. Kahvecioglu, Y. Yoo, J.-W. T. Seo, J. R. Downing, H.-D. Lim, M. J. Bedzyk, C. Wolverton and M. C. Hersam, *Adv. Mater.*, 2022, **34**, 2106402.
48 P. Xiao, T. Shi, W. Huang and G. Ceder, *ACS Energy Lett.*, 2019, **4**, 811–818.
49 P. Mukherjee, N. V. Faenza, N. Pereira, J. Ciston, L. F. J. Piper, G. G. Amatucci and F. Cosandey, *Chem. Mater.*, 2018, **30**, 8431–8445.
50 D. P. Abraham, R. D. Twesten, M. Balasubramanian, J. Kropf, D. Fischer, J. McBreen, I. Petrov and K. Amine, *J. Electrochem. Soc.*, 2003, **150**, A1450.
51 D. P. Abraham, R. D. Twesten, M. Balasubramanian, I. Petrov, J. McBreen and K. Amine, *Electrochem. Commun.*, 2002, **4**, 620–625.
52 F. Lin, I. M. Markus, D. Nordlund, T.-C. Weng, M. D. Asta, H. L. Xin and M. M. Doeff, *Nat. Commun.*, 2014, **5**, 3529.
53 S. Zheng, R. Huang, Y. Makimura, Y. Ukyo, C. A. J. Fisher, T. Hirayama and Y. Ikuhara, *J. Electrochem. Soc.*, 2011, **158**, A357.
54 A. Mikheenkova, S. Mukherjee, M. Hirsbrunner, P. Törnblom, C.-W. Tai, C. U. Segre, Y. Ding, W. Zhang, T. C. Asmara, Y. Wei, T. Schmitt, H. Rensmo, L. Duda and M. Hahlin, ChemRxiv.
55 J. Wandt, A. T. S. Freiberg, A. Ogrodnik and H. A. Gasteiger, *Mater. Today*, 2018, **21**, 825–833.
56 D. H. Seo, J. Lee, A. Urban, R. Malik, S. Kang and G. Ceder, *Nat. Chem.*, 2016, **8**, 692–697.
57 W. M. Dose, W. Li, I. Temprano, C. A. O'Keefe, B. L. Mehdi, M. F. L. De Volder and C. P. Grey, *ACS Energy Lett.*, 2022, **7**, 3524–3530.
58 B. Strehle, K. Kleiner, R. Jung, F. Chesneau, M. Mendez, H. A. Gasteiger and M. Piana, *J. Electrochem. Soc.*, 2017, **164**, A400.
59 X. Chen, N. Li, E. Kedzie, B. D. McCloskey, H. Tang and W. Tong, *J. Electrochem. Soc.*, 2019, **166**, A4136.
60 R. Jung, M. Metzger, F. Maglia, C. Stinner and H. A. Gasteiger, *J. Electrochem. Soc.*, 2017, **164**, A1361–A1377.
61 R. Sharpe, R. A. House, M. J. Clarke, D. Förstermann, J.-J. Marie, G. Cibin, K.-J. Zhou, H. Y. Playford, P. G. Bruce and M. S. Islam, *J. Am. Chem. Soc.*, 2020, **142**, 21799–21809.
62 R. A. House, U. Maitra, M. A. Pérez-Osorio, J. G. Lozano, L. Jin, J. W. Somerville, L. C. Duda, A. Nag, A. Walters, K.-J. Zhou, M. R. Roberts and P. G. Bruce, *Nature*, 2020, **577**, 502–508.
63 K. Chai, J. Zhang, Q. Li, D. Wong, L. Zheng, C. Schulz, M. Bartkowiak, D. Smirnov and X. Liu, *Small*, 2022, **18**, 2201014.
64 E. Boivin, R. A. House, M. A. Pérez-Osorio, J.-J. Marie, U. Maitra, G. J. Rees and P. G. Bruce, *Joule*, 2021, **5**, 1267–1280.
65 U. Maitra, R. A. House, J. W. Somerville, N. Tapia-Ruiz, J. G. Lozano, N. Guerrini, R. Hao, K. Luo, L. Jin, M. A. Pérez-Osorio, F. Massel, D. M. Pickup, S. Ramos, X. Lu, D. E. McNally, A. V. Chadwick, F. Giustino, T. Schmitt, L. C. Duda, M. R. Roberts and P. G. Bruce, *Nat. Chem.*, 2018, **10**, 288–295.
66 R. A. House, J.-J. Marie, J. Park, G. J. Rees, S. Agrestini, A. Nag, M. Garcia-Fernandez, K.-J. Zhou and P. G. Bruce, *Nat. Commun.*, 2021, **12**, 2975.

